Surface creep rate and moment accumulation rate along the Aceh segment of the Sumatran fault from L-band ALOS-1/PALSAR-1 observations

X. Tong[1], D. T. Sandwell[2], and D. A. Schmidt[1]

[1]Department of Earth and Space Sciences, University of Washington (Seattle) U.S.A.
[2]Scripps Institution of Oceanography, University of California San Diego, U.S.A.

Corresponding author: Xiaopeng Tong (xitong@uw.edu)

Key points:

1. We processed ALOS-1 data with a coherence-based InSAR time-series method to image the inter-seismic deformation along the Sumatran fault.
2. The InSAR observation reveals up to ~20 mm/yr of creep along a 100 km long section of the Aceh segment.
3. We estimated the moment accumulation rate of this fault segment.

This article has been accepted for publication and undergone full peer review but has not been through the copyediting, typesetting, pagination and proofreading process which may lead to differences between this version and the Version of Record. Please cite this article as doi: 10.1002/2017GL076723

Abstract

We analyzed the InSAR data from the ALOS-1/PALSAR-1 satellite to image the interseismic deformation along the Sumatran fault. The InSAR time-series analysis reveals up to ~20 mm/yr of aseismic creep on the Aceh segment along the Northern Sumatran fault. This is a large fraction of the total slip rate across this fault. The spatial extent of the aseismic creep extends for ~100 km. The along-strike variation of the aseismic creep has an inverse "U" shape. An analysis of the moment accumulation rate shows that the central part of the creeping section accumulates moment at approximately 50% of the rate of the surrounding locked segments. An initial analysis of temporal variations suggests that the creep rate may be decelerating with time, suggesting that the creep rate is adjusting to a stress perturbation from nearby seismic activity. Our study has implications to the earthquake hazard along the northern Sumatran fault.

1. Introduction

The fast subduction (~ 40-60 mm/yr) of the Indo-Australia plate underneath the Sunda microplate drives the regional tectonics in southwest Asia. The detachment of the forearc blocks from the overriding plate leads to slip partitioning at this highly oblique subduction zone [*McCaffrey*, 1992]. Deformation in the western Indonesia is characterized by right-lateral motion of the Sumatran fault and the oblique subduction of the Sumatra-Java trench. The tectonics of Sumatra is a classic example of slip partitioning, where margin-parallel motion between two obliquely converging plates is taken up on multiple parallel crustal faults.

The Sumatran fault is highly segmented, right-lateral transform fault, running through a chain of volcanoes. The Aceh segment of the Sumatran fault runs in the northwest-southeast direction along the Barisan mountain range. The fault geometry and topography are complex in this region. In the north, the Sumatran fault branches into a parallel fault called Seulimeum fault (Figure 1). To the south it branches into the Batee segment. A northwest increase in the geological slip rate: from 11 mm/yr between 0-3.5S to 28 mm/yr near 2.2N manifests in the transtensional deformation of the forearc [*Sieh and Natawidjaja*, 2000]. GPS observations have revealed that the plate motion is composed of convergence directed normal to the megathrust fault (Mentawai segment of the Sunda trench) and right-lateral strike-slip motion along the 1900 km long Sumatra fault. The strain-rates on the Sumatran is estimated to be around 5e10^-8 to 1e-7 with minor clock-wise rotation [*Bock et al*., 2003]. More recently, a new block model and new GPS observations along the Sumatran subduction zone have significantly improved our understanding on the interseismic coupling of the megathrust and the interseismic deformation along the Great Sumatran fault [*Prawirodirdjo et al.,* 2010].

Advanced Interferometric Synthetic Aperture Radar (InSAR) techniques have been used to provide high-resolution line-of-sight (LOS) velocity maps along active fault systems [*Fialko*, 2006; *Tong et al*., 2013; *Elliott et al*., 2016]. These continuous velocity fields mapped by InSAR can characterize the interseismic period of the earthquake cycle deformation. InSAR observations have proven to be effective to constrain the fault slip rates and the aseismic creep rates where GPS observations are sparse. The first InSAR time series survey of the Sumatran island was focused on the deformation of the volcanic arc and localized subsidence in anthropogenic regions [*Chaussard and Amelung*, 2012; *Chaussard et al*., 2013]. The Sumatra Island sits in a tropical rain forest and temporal decorrelation poses a challenge for InSAR studies. L-band observation from Advanced Land Observing Satellite (ALOS-1) is effective at recovering surface deformation in highly vegetated regions such as the Sumatran volcanic arc [*Chaussard and Amelung*, 2012; *Chaussard et al*., 2013]. While these studies focused on the volcanic arc, the tectonic deformation along the Sumatran fault has not been studied in detail. A GPS network was established in the northern portion of the Sumatran fault [*Ito et al*., 2012], and they found evidence of shallow aseismic creep and deeper locking on the Aceh segment.

In this study, our goal is to recover the interseismic deformation of the Sumatran fault and to assess earthquake hazard of this region. Of particular interests is to investigate the moment accumulation rate of the creeping fault segment. InSAR provides a surface velocity field along the Sumatran fault and the along-strike variations of the aseismic fault creep. To improve signal recovery, we implement an improved InSAR time-series method that incorporates the coherence of the interferograms as weights.

2. Data analysis

The data used in this study comes from the ALOS-1 satellite and spans the time period from 2007 to 2010 (Table S1). In tropical regions such as Sumatra, vegetation poses a serious problem for InSAR because of temporal decorrelation [*Wei and Sandwell*, 2010]. The L-band radar onboard ALOS-1 has the advantage of maintaining temporal correlation over a longer period of time compared to the radar systems that use a shorter signal wavelength. Depending on the path and frame, the baseline of the ALOS-1 satellite drifted over a range of up to 7000 m during the satellite's time in orbit. However, as shown in the baseline-time plot (Figure S1), the baseline of ALOS-1 does not drift significantly over the Sumatra region, thereby improving the quality of interferograms.

We produced differential interferograms using an open source InSAR processing system GMTSAR [*Sandwell et al*., 2011]. Interferograms are selected such that their temporal baseline is smaller than 3 years and their spatial baseline is smaller than 1500m. All the SAR images are co-registered to a single master scene using a batch processing approach [*Tong et al*., 2013]. The phase signals from the topography are removed based on the SRTM30 DEM [*Farr and Kobrick*, 2000]. These interferograms are then unwrapped with the phase unwrapping method SNAPHU [*Chen and Zebker*, 2008]. Because the phase of the

interferogram is sparse, we implemented an advanced resampling algorithm to facilitate phase unwrapping [*Agram and Zebker*, 2009].

We examined the differential interferograms visually and found instances of anomalous phase patterns attributable to the ionosphere. L-band radar is sensitive to the variability of the Total Electron Content within the ionosphere [*Gomba et al*., 2015]. In equatorial regions, interferograms commonly exhibit stripes aligned in the direction of the earth's magnetic field. We attempted to exclude interferograms with obvious ionospheric noise. For example, 29 ionosphere-contaminated interferograms associated with 6 SAR images were removed (Figure S2). The remaining 37 interferograms were then used to construct LOS time series using the SBAS algorithm [*Schmidt and Bürgmann*, 2003].

We implemented a newly developed InSAR time-series processing method to extract the interseismic LOS velocity from the interferometric phase observations. We have improved the conventional SBAS methodology by including the decorrelation information of the interferograms [*Tong and Schmidt*, 2016]. Instead of discarding the noisy phase data present in a fraction of the interferograms, we keep all the pixels in the processing chain and weight the observed phase data based on the correlation using a covariance matrix. This weighting scheme results in a spatially coherent signal with dense coverage and improved precision. We will compare the results with and without the coherence in the following section.

We reduced the ALOS-1/PALSAR-1 interferograms to interseismic LOS velocities along the Sumatran Fault using a remove/restore method [*Tong et al*., 2013]. We corrected for the noise with long wavelength, possibly due to orbital, atmospheric and ionospheric errors, using a tectonic block model. *Prawirodirdjo et al.* [2010] developed an elastic model of the horizontal interseismic velocity field based on GPS observations in the entire Sumatra region. The model consists of both the subduction fault and the Sumatran Fault. Because new GPS observations has shown that the Aceh segment is slipping at faster slip rates [*Ito et al*., 2012], we have updated the model by increasing the long-term fault slip rate between the Sunda and the Central Sumatra block to 31 mm/yr when predicting the horizontal interseismic velocity field [*Prawirodirdjo et al.* 2010]. This model is used to calculate the averaged long-term velocity field along the Sumatran Fault. We applied a spatial filter with 60 km wavelength to the InSAR data in the remove/restore method. The filter wavelength can be chosen by considering the spatial scale of the surface deformation signal and the noise in the InSAR observations. In a previous study at the San Andreas Fault we have determined the wavelength to be 40 km by comparing multiple GPS-based deformation models [*Tong et al*., 2013]. We also show an InSAR LOS interseismic velocity map without the block model correction in the supporting information (Figure S3).

3. Results

The InSAR-derived LOS velocity map reveals the relative deformation along the entire Sumatran fault from 2007-2010. (Figure 1a). The positive LOS values indicate a range

decrease and the negative values indicate a range increase. The discontinuities in the InSAR velocity map coincide with the mapped fault trace of the Sumatran fault [*Sieh and Natawidjaja*, 2000]. Near the Aceh segment, the LOS velocity jumps from 5 to 15 mm/yr, which is equivalent to ~20 mm/yr of right-lateral strike-slip motion assuming there is no vertical motion across the fault. The step-like change in velocity across the fault on the Aceh segment suggests that shallow aseismic fault creep prevails. The creep signal along the northern portion of the Aceh segment is not as clear as the southern part of the Aceh segment. This coincides with the branching of the Seulimeum fault.

The fault creep rate is estimated by applying linear regression to the velocity profiles on both sides of the Sumatran fault following the methodology of *Tong et al*. [2013]. We took cross profiles of the LOS velocities at 0.5 km interval for 5 km on both sides of the fault. Then we combined multiple profiles by a median filter. Every 10 km we obtain a single LOS velocity profile. The profiles can be fit by two linear functions on either side of the fault. The noisy profiles with a low signal-to-noise ratio are removed. The linear function yields two intercepts and the difference of these intercepts is the final estimate of the fault creep signal (Figure 1b). We assume that the velocity offsets in the InSAR LOS profiles are due to right-lateral strike-slip motion along the surface trace of the Sumatran fault. The error bars are estimated by calculating the variance of the residuals. This method of estimating fault creep rate has been applied to study the fault creep of the entire San Andreas Fault, and we found the result from this linear regression method compared well with the ground-based instruments such as alignment arrays and GPS [*Tong et al*., 2013].

The creep rate is close to zero at the northern-most part of the Aceh segment where it branches into the Seulimeum segment, and it increases gradually towards the southeast. The maximum observed creep rate is about 22 mm/yr and it is approximately in the center of the fault segment (latitude 4.7-4.8 deg). Then it decreases to zero at latitude 4.2 deg, which is to the south of the Batee segment. The length of the Aceh segment that exhibits aseismic slip behavior extends approximately 110-120 km. The overall shape of the creep rate resembles an inversed "U", which is very similar to the creep signal found along the central creeping section of the San Andreas Fault [*Tong et al*., 2013] and the Ismetpasa segment of the North Anatolian fault [*Kaneko et al*., 2013]. Campaign GPS surveys crossing the Aceh fault segment were conducted from 2005 to 2009 [*Ito et al*., 2012]. Two profiles measured the velocity variations across the fault. The northern profile shows 20 mm/yr of right-lateral creep and the southern profile shows no creep (Figure 2c). Our result is in excellent agreement with the GPS data in the northern profile. The difference in the estimated creep rates in the southern profile could be attributed to the time-dependence of the fault creep.

South of the Aceh segment, the creep rates estimates are more noisy and there is no convincing evidence of fault creep from the InSAR results. We interpolated the creep rate data with 1D spline. The creep data in the Aceh segment can be well fit by the spline curve while the data in the south are more scattered. Data outliers can be removed with the spline. To better quantify the uncertainty in the InSAR-inferred creep rates, we calculated the average of the standard deviations of the creep rate estimates to be approximately 5 mm/yr,

which provides a good estimate of the level of the noise in the data. If the data scatter around 5 mm/yr and doesn't show a consistent pattern, we interpret the associated fault segment to be locked. Figure 1c shows our interpretation on the distribution of the creeping and locked segment along the Sumatran Fault.

To illustrate the effectiveness of the coherence-based SBAS, we performed the traditional SBAS analysis using the same differential interferograms but without applying the weighting scheme (Figure 2). The derived velocity map without weighting is less coherent and contains additional scatter. The decorrelated pixels have large phase outliers in the least-square inversion of the InSAR time–series analysis. A careful treatment of the covariance matrix will down-weight the outliers and result in a more robust estimate of the incremental displacement time-series and a more robust velocity estimates. Figure 2c shows three cross-sections of the LOS velocity perpendicular to the Aceh segment. The coherence-based SBAS results (black lines) are significantly smoother than the traditional SBAS results (blue lines). A comparison of the LOS displacement time-series from the two methods is shown in the supporting information (Figure S4).

Our InSAR results help to extend the spatial coverage provided by the sparse GPS data for the region, and allow us to constrain the moment accumulation rate along the Aceh segment to better understand the seismic hazards along this creeping fault. *Maurer et al*. [2017] rigorously investigated the methods to constrain the bounds of the moment deficit rate from geodetic observations. They proposed two new methods, Constrained Optimization Bounding Linear Estimator (COBLE) and Constrained Optimization Bounding Estimator (COBE), and studied the Parkfield region of the San Andreas Fault.

Extending the approach by *Maurer et al*. [2017], we have developed an integral method to estimate the moment accumulation rate of a fault segment. This method builds upon an accurate and continuous surface velocity field and it can only be applied to the case of a vertical strike-slip fault. The principle of the method is given by the following formula. The moment accumulation rate of a given fault segment, $\dot{M}$, is directly related to the integral of the residual velocity, $v(x)$, times the distance from the fault, x. L is the length of the fault segment. W is the distance limit of the integral across the fault trace and D_m is the locking depth of the fault segment [*Tong et al.*, 2015]. μ is the shear modulus of the crust. Note that we found and corrected a factor of two errors in the original derivation.

$$\frac{\dot{M}}{L} = \lim_{W\to\infty} \frac{\mu\pi}{2W} \int_{-W}^{W} xv(x)dx \,, W \gg D_m \qquad (1)$$

In this calculation, the integral needs to be carried out over a large fault-perpendicular distance, at least several locking depth away from the fault trace. The along-strike variation of the moment accumulation rate is obtained by integration of multiple profiles across the fault trace. As pointed out in *Maurer et al*. [2017], this integral method is less robust because

it might suffer from convergence issue, due to a limit in the spatial coverage of the InSAR data. Another more commonly used method is to estimate the creep rate and creep depth in a 2D screw dislocation model and calculate the moment accumulation rate from the best-fit model parameters [e.g., *Savage and Lisowski*, 1993].

We applied both the integral method and the dislocation model to resolve the moment accumulation rate along the Aceh segment and compare their results. We took 6 cross-profiles of the InSAR interseismic LOS velocity map and developed 6 best-fit dislocation models respectively (Figure S5 and S6). In developing the model we assume the fault slip rate is 31 mm/yr and the locking depth is 14 km [*Ito et al*., 2012]. The creep rate is well resolved from InSAR (Figure 3a). The depth extent of the creep is set to be the free parameter for the dislocation models. We vary the creep depth from 0 to 12 km and search for the best-fit model that yields the smallest misfit (Figure 3b). Interestingly we found that the depth extent of the fault creep is not uniform. The analysis infers that the creep depth is shallower in the southern part of the creeping Aceh fault segment (4 km depth) and deeper in the northern part of it (8-10 km depth). From the creep rate, creep depth, slip rate and locking depth we estimate the moment accumulation rate for each profile. The along-strike variation of the moment accumulation rate is shown as the black line in Figure 3c. The result from the integral method is shown as the blue line in Figure 3c. We found that two independently estimated moment accumulation rates agree with each other to the first order. The integral method is sensitive to the noise in the velocity profile, and it depends on a reliable estimate of an accurate and continuous InSAR velocity map. From Figure 3c, we found the moment accumulation rate is inversely proportional to the fault creep rates; the moment accumulates slower where the fault creeps faster. The fault creep releases moment aseismically, and thus it reduces the rate of moment accumulation. There is no significant surface creep on the locked ends of the fault segment. Thus we assume the Sumatran fault is fully locked on both sides of the creeping Aceh segment, as shown in Figure 3.

4. Discussions

Previous studies on the fault slip rates along the Aceh segment of the Sumatran Fault have shown that this region is tectonically active. Geological studies have shown a northward increase in slip rates along the Sumatran Fault [*Bennett et al*. 1981; *Sieh and Natawidjaja*, 2000]. The geologic slip rate of the northern part of the Sumatra fault is found to be 27 mm/yr by *Sieh et al*. [1994] and 38 mm/yr by *Bennett* [1981]. *Genrich et al.* [2000] investigated the slip partitioning and forearc deformation with GPS observations. Their study yielded a slip rate of 5+-2 mm/yr along the Aceh segment based on a small aperture array at the northern tip of the Aceh segment from 5.4-5.6 deg north. A continuous and campaign GPS network (AGNeSS) has been installed in the northern Sumatran area in 2005, after the destructive 2004 Sumatra-Andaman earthquake [*Ito et al*., 2012]. *Ito et al*. [2012] inferred a slip rate of 20+-6 mm/yr based on new GPS observations of the Aceh segment. In our moment accumulation rate estimation we have improved the block model from [*Prawirodirdjo et al*., 2010] by assuming the slip rate of the northern segment to be 31

mm/yr.

Sieh and Natawidjaja [2000] have documented large historical earthquakes on all the major segments of the Sumatran Fault. They found that the 200 km long Aceh segment has no record of significant earthquakes. This would suggest that the fault strain on this segment has not been released seismically. Our finding of the aseismic fault creep and its moment accumulation rate has implications to the earthquake hazard assessment in this region. Since moment is accumulating and the fault is not creeping at its full strike-slip plate tectonic rate during our observation period, there is a possibility some strain could be released seismically on the creeping segment. *Kaneko et al*. [2010] has inferred dynamic patterns of earthquake rupture from scenarios of interseismic coupling. The moment accumulation rate provides spatial information on the magnitude of earthquake that could potentially occur on a fault segment, which could be used as an additional input to parameterizations of dynamic models of earthquake propagation.

The 2004 Sumatra earthquake has generated widespread post-seismic deformation [*Pollitz et al*., 2006; *Gahalaut et al.,* 2008]. The estimated interseismic velocity and the fault creep rate from InSAR are approximately four years after the 2004 Sumatra mega-thrust earthquake. *Ito et al.* [2012] presented the time-series of the post-seismic displacements from GPS. Their study found that the GPS time-series data could be explained by an afterslip model of rate-strength brittle creep following the major subduction zone events and the relaxation time is around 8.76 years. The InSAR data could potentially be affected by the post-seismic effect following the great 2004 Sumatra earthquake.

We investigated the time-dependence of the InSAR-derived interseismic LOS velocity. We took the difference between two points directly on either side of the Sumatran fault. These two points are approximately 2 km away from the fault (one point is at 96.193, 4.780 and the other point is at 96.161, 4.748) so they are most sensitive to shallow fault creep. Figure 4 shows the differential LOS displacement across the fault as a function of time. The data exhibit an increase in relative displacement. We fit a linear model and a quadratic model for comparison. Both the models can fit the data well. The best-fit quadratic model has a slightly smaller misfit compared to the best-fit linear model, but it is not significantly different from the linear model. The time span of the InSAR data is limited to approximately 4 years and it cannot completely distinguish the linear model from the more complex time-dependent model. More InSAR observations that span a longer time period is needed to resolve the time-dependence of fault creep [*Lienkamper et al.*, 1997; *Schmidt and Bürgmann*, 2008].

5. Conclusions

In summary, we processed ALOS-1/PALSAR-1 data along the ascending orbits to image the interseismic LOS velocity field along the Sumatran fault. We applied a coherence-based

SBAS method particularly suitable for retrieving signals in vegetated regions. InSAR detected active deformation along the Sumatran fault, in particular, the active fault creep rate along the Aceh segment of the Sumatran fault reaches around 20mm/yr. The along-strike variation of the aseismic creep has an inversed "U" shape. And we have used the integral method and dislocation models to estimate the moment accumulation rate of the creeping Aceh segment.

Acknowledgements

We thank Yoshi Kaneko for his constructive comments on an early draft of the manuscript. The L-band ALOS-1 data are provided by the Japanese Aerospace and Exploration Agency (JAXA) under a research project "Interseismic deformation of the Sumatra fault, Indonesia" (PI number 1105). The interseismic InSAR Line-Of-Sight velocity field and the model results are available at the following ftp site: ftp://topex.ucsd.edu/pub/sumatra. Figures are made with GMT [*Wessel et al*., 2013]. This work was partially supported by the NASA Earth Surface and Interior Program (NNX16AK93G).

References

Agram, P. S. and H. A. Zebker (2009), Sparse Two-Dimensional Phase Unwrapping Using Regular-Grid Methods, IEEE GEOSCIENCE AND REMOTE SENSING LETTERS, VOL. 6, NO. 2.

Bennett, J. D., et al. (1981), Geologic map of Banda Aceh Quadrangle, North Sumatra, 1:250000, Geol. Res. and Dev. Cent., Bandung, Indonesia.

Chaussard, E., F. Amelung, and Y. Aoki (2013), Characterization of open and closed volcanic systems in Indonesia and Mexico using InSAR time series, J. Geophys. Res. Solid Earth, 118, 3957–3969, doi:10.1002/jgrb.50288.

Chaussard, E., and F. Amelung (2012), Precursory inflation of shallow magma reservoirs at west Sunda volcanoes detected by InSAR, Geophys. Res. Lett., 39, L21311, doi:10.1029/2012GL053817.

Chen, C. W., and H. A. Zebker (2000), Network approaches to two-dimensional phase unwrapping: Intractability and two new algorithms, J. Op. Soc. Am. A Op., Image Sci., 17(3), 401–414, doi:10.1364/ JOSAA.17.000401.

Elliott, J. R., R. J. Walters, and T. J. Wright (2016), The role of space-based observation in understanding and responding to active tectonics and earthquakes. Nature communications, 7, 13844.

Farr, T. G., and M. Kobrick (2000), Shuttle radar topography mission produces a wealth of data, Eos Trans. AGU, 81(48), 583–585, doi:10.1029/EO081i048p00583.

Fialko, Y. (2006). Interseismic strain accumulation and the earthquake potential on the southern San Andreas Fault system. In: Nature 441.7096, p. 968.

Genrich, J.F., Y. Bock, R. McCaffrey, L. Prawirodirdjo, C. W. Stevens,

S. O. Puntodewo, C. Subarya, and S. Wdowinski (2000), Distribution of slip at the northern Sumatran fault system, Journal of Geophysical Research, Vol. 105, No. B12, Pages 28,327-28,341

Gahalaut, V. K., et al. (2008), GPS measurements of postseismic deformation in the Andaman Nicobar region following the Giant 2004 Sumatra-Andaman earthquake, J. Geophys. Res., 113, B08401, doi:10.1029/2007JB005511.

Gomba G., A. Parizzi, F. De Zan, M. Eineder and R. Bamler (2015), Towards observational compensation of ionosphere effects in SAR interferograms: the split-spectrum method, IEEE on Geoscience and Remote Sensing, 10.1109/TGRS.2015.2481079.

Ito, T., E. Gunawan, F. Kimata, T. Tabei, M. Simons, I. Meilano, Agustan, Y. Ohta, I. Nurdin, and D. Sugiyanto (2012), Isolating along-strike variations in the depth extent of shallow creep and fault locking on the northern Great Sumatran Fault, J. Geophys. Res., 117, B06409, doi:10.1029/2011JB008940.

Kaneko, Y., J. P. Avouac, and N. Lapusta, (2010). Towards inferring earthquake patterns from geodetic observations of interseismic coupling, *Nat. Geosci.*, **3**(5), 363–369.

Kaneko, Y., Y. Fialko, D. T. Sandwell, X. Tong, M. Furuya, (2013), Interseismic deformation and creep along the central section of the North Anatolian fault (Turkey): InSAR observations and implications for rate-and-state friction properties. Journal of Geophysical Research, 118(1): 316-331; doi: 10.1029/2012JB009661

Lienkamper J. J., J. S. Galehouse, R.W.Simpson (1997), Creep response of the Hayward fault to stress changes caused by the Loma Prieta earthquake, Science, doi:10.1126/science.276.5321.2014

Maurer, J., P. Segall, and A. M. Bradley (2017). Bounding the moment deficit rate on crustal faults using geodetic data: Methods. Journal of Geophysical Research: Solid Earth.

McCaffrey, R. (1992). Oblique plate convergence, slip vectors, and forearc deformation. Journal of Geophysical Research: Solid Earth, 97(B6), 8905-8915.

Prawirodirdjo, L., R. McCaffrey, C. D. Chadwell, Y. Bock, and C. Subarya, Geodetic observations of an earthquake cycle at the Sumatra subduction zone: Role of interseismic strain segmentation (2010), Journal of Geophysical Research, Vol. 115, B03414, doi:10.1029/2008JB006139

Pollitz, F. F., R. Bürgmann, and P. Banerjee (2006), Post-seismic relaxation following the Great 2004 Sumatra-Andaman earthquake on a compressible self-gravitating Earth, Geophys. J. Int., 167, 397–420.

Sandwell, D., R. Mellors, X. Tong, M. Wei, and P. Wessel (2011), Open radar interferometry software for mapping surface deformation, Eos Trans. AGU, 92(28), doi:10.1029/2011EO280002

Savage J.C., M. Lisowski (1993), Inferred depth of creep on the Hayward fault, Central California, Journal of Geophysical Research, Vol. 98, No. B1, 787-793, Doi: 10.1029/92JB01871.

Schmidt, D.A. and R. Bürgmann (2003), Time-dependent land uplift and subsidence in the Santa Clara valley, California, from a large interferometric synthetic aperture radar data set. J. Geophys. Res. 108 (B9), 2416. http://dx.doi.org/10.1029/2002JB002267.

Schmidt, D. A. and R. Bürgmann (2008), Predicted reversal and recovery of surface creep on the Hayward fault following the 1906 San Francisco earthquake, Geophysical Research Letters, Vol. 35, L19305, doi:10.1029/2008GL035270

Sieh, K. and J. Zachariasen, Y. Bock, L. Edwards, F. Taylor, and P. Gans (1994), Active tectonics of Sumatra, Geol. Soc. Am. Abstr. Programs, 26, 382.

Sieh, K., and D. Natawidjaja (2000), Neotectonics of the Sumatran fault, Indonesia, J. Geophys. Res., 105, 28,295-28,326, doi:10.1029/2000JB900120

Tong, X., D. T. Sandwell and B. Smith-Konter (2013), High resolution interseismic velocity data along the San Andreas fault from GPS and InSAR, J. Geophys. Res., 118, doi:10.1029/2012JB009442.

Tong X., B. Smith-Konter and D. T. Sandwell (2014), Is there a discrepancy between geologic and geodetic slip rates along the San Andreas Fault System?, Journal of Geophysical Research-solid earth, doi:10.1002/2013JB010765.

Tong, X., D. T. Sandwell, & B. Smith-Konter (2015), An integral method to estimating the moment accumulation rate on the creeping section of the San Andreas Fault. *Geophys. J. Int.* 203, 48–62.

Tong X., D. Schmidt (2016), Active movement of the Cascade Landslide Complex from a coherence-based InSAR time-series method, Remote Sensing of Environment. Volume 186, 1 December 2016, Pages 405-415. https://doi.org/10.1016/j.rse.2016.09.008.

Wei, M., and D. T. Sandwell (2010). Decorrelation of L-band and C-band interferometry over vegetated areas in California. *IEEE Transactions on Geoscience & Remote Sensing*, *48*(7), 2942-2952.

Wessel, P., W. H. F. Smith, R. Scharroo, J. F. Luis, and F. Wobbe (2013), Generic mapping tools: Improved version released, EOS Trans. AGU, 94, 409–410,

doi:10.1002/2013EO450001.

Figures

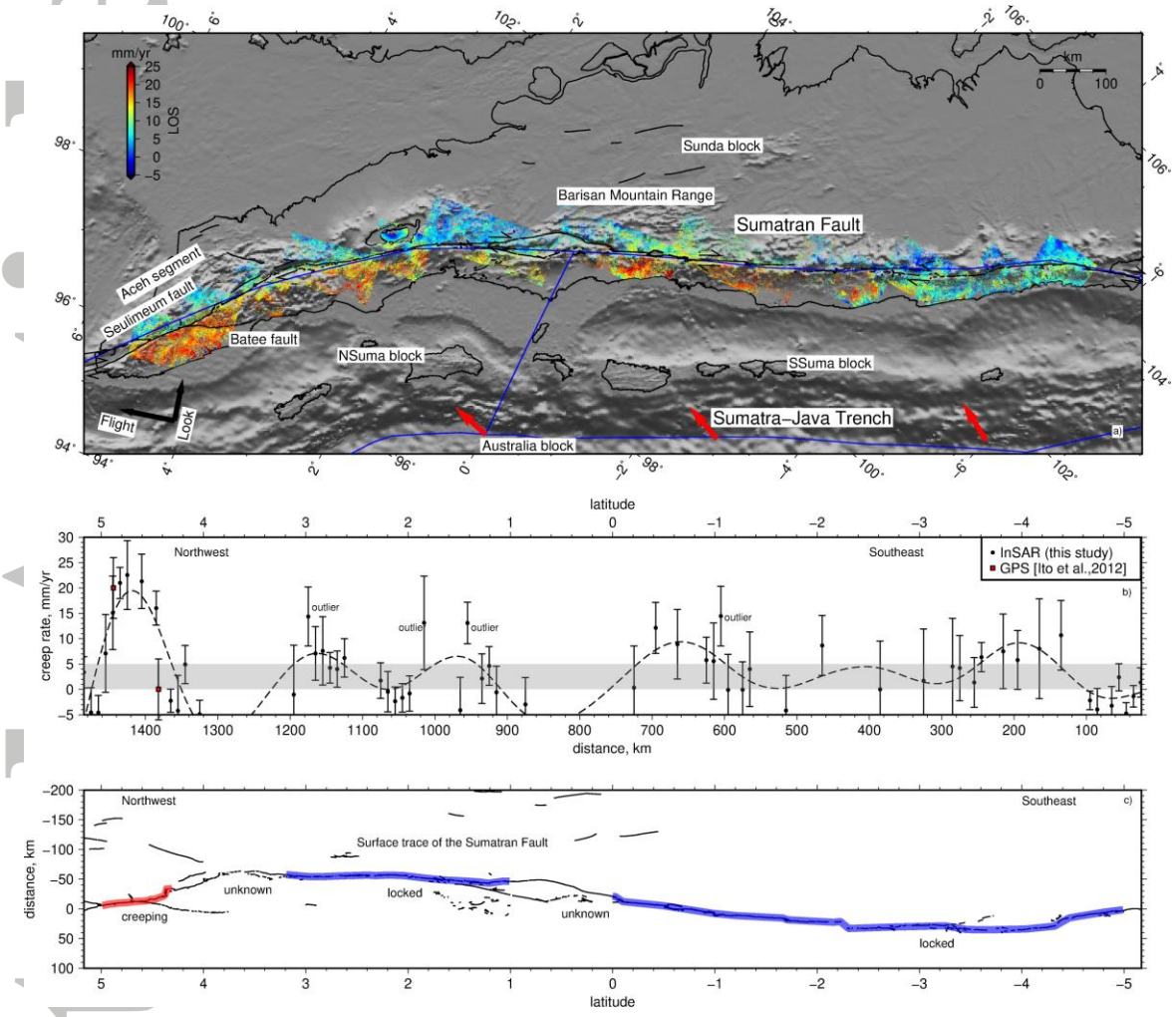

Figure 1. a) InSAR Line-Of-Sight (LOS) interseismic velocity map along the Sumatran Fault from ALOS-1/PALSAR-1 observations. Areas with high vegetation-induced decorrelation are masked. Blue lines outline the boundary of the block model [*Prawirodirdjo et al*., 2010]. Red vectors indicate the relative plate motion between the Australia plate and the Sunda microplate. Thin black lines denote the surface trace of the Sumatran Fault. b) Fault creep rate variation along the Sumatran Fault estimated from InSAR. It is compared with GPS (*Ito et al*. [2012]). The distance is calculated starting at the southeastern end of the Sumatran Fault and it increases northward. The uncertainty of the InSAR-derived fault creep is estimated at 5 mm/yr (gray band). c) Surface trace of the Sumatran Fault with interpretations on the distribution of the predominately locked and creeping segments.

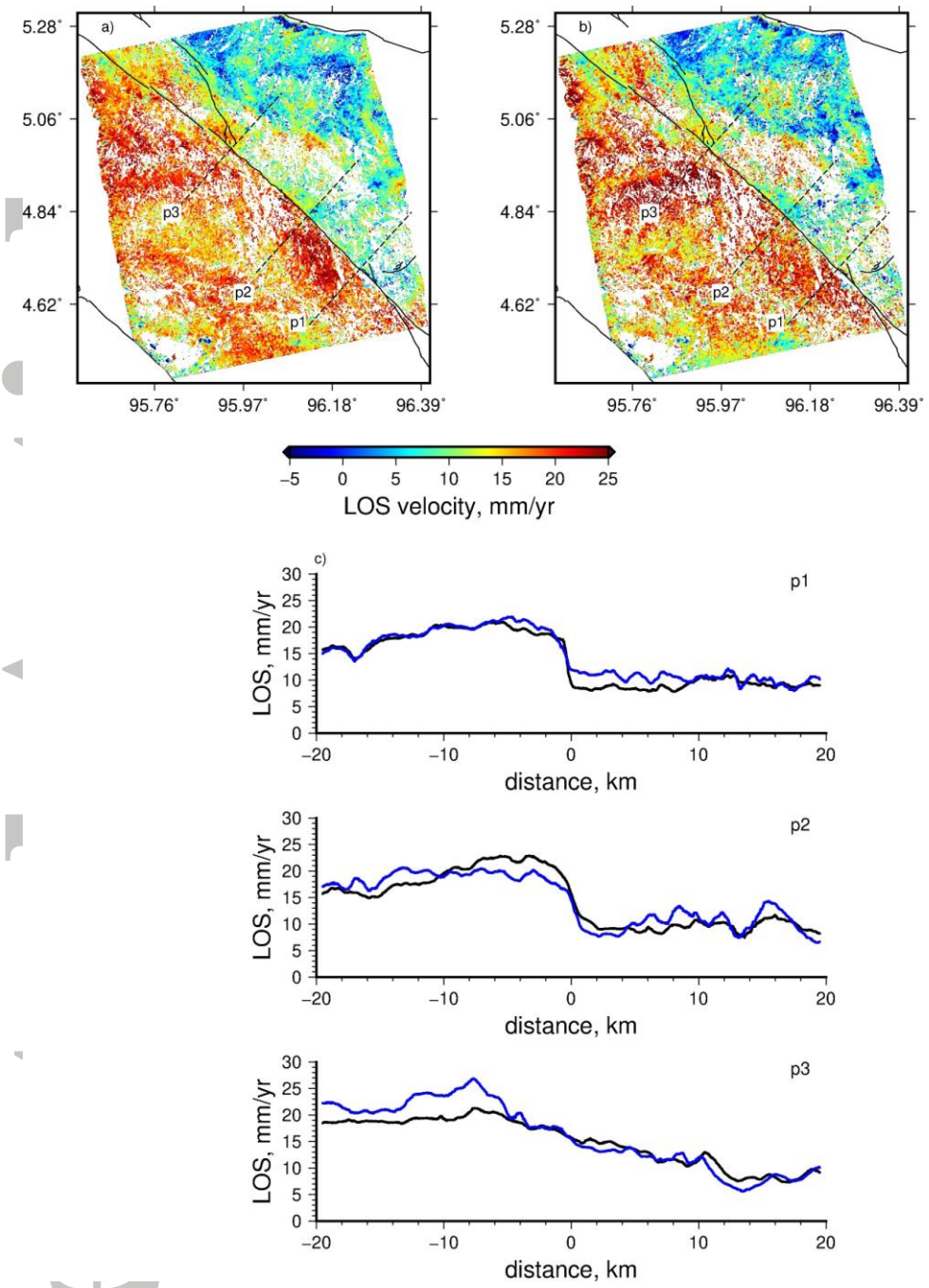

Figure 2. Comparison on the coherence-based InSAR time-series method and the no-coherence-weighting InSAR time-series method. This example is from Track 499 Frame 0800 along the Aceh segment of the Sumatran fault (see Figure 1). a) InSAR LOS velocity from the coherence-based InSAR time-series method. b) InSAR LOS velocity from the no-coherence-weighting method. The locations of the three profiles are shown. c) InSAR LOS velocity profiles perpendicular to the Sumatran fault. The black lines are from the coherence-based method and the blue lines are the results from the no-coherence-weighting method.

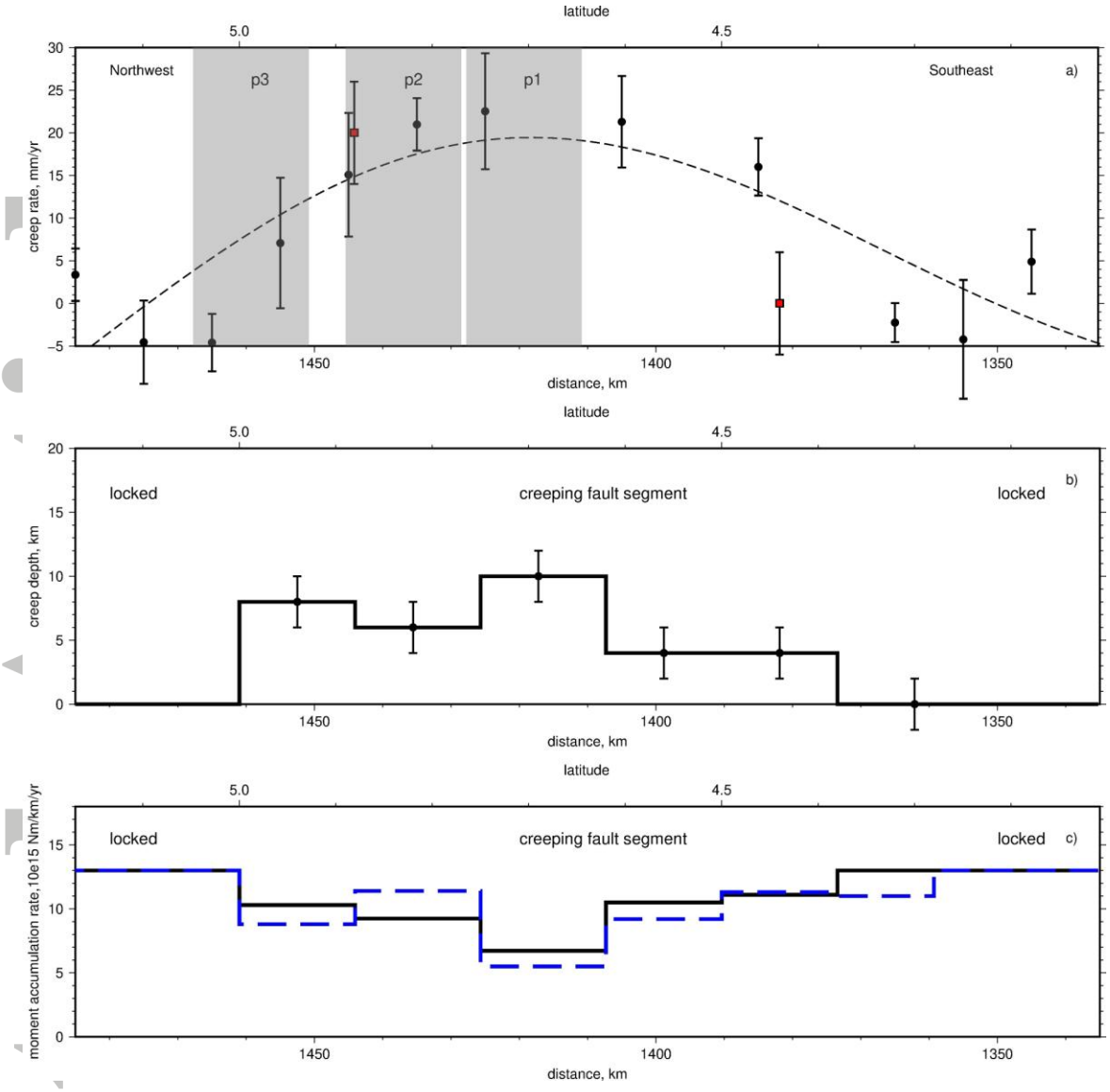

Figure 3. a) Along-strike variation of the creep rate of the Aceh segment (see Figure 1 and Figure 2). The location and coverage of the profiles in Figure 2 are marked by the gray bands. b) Variation of the depth extent of fault creep estimated from fault-perpendicular profiles of the InSAR LOS velocity. c) Moment accumulation rate variation along fault-strike. The black line is the moment accumulation rate estimated by 2D dislocation models and the blue line is estimated by the integral method.

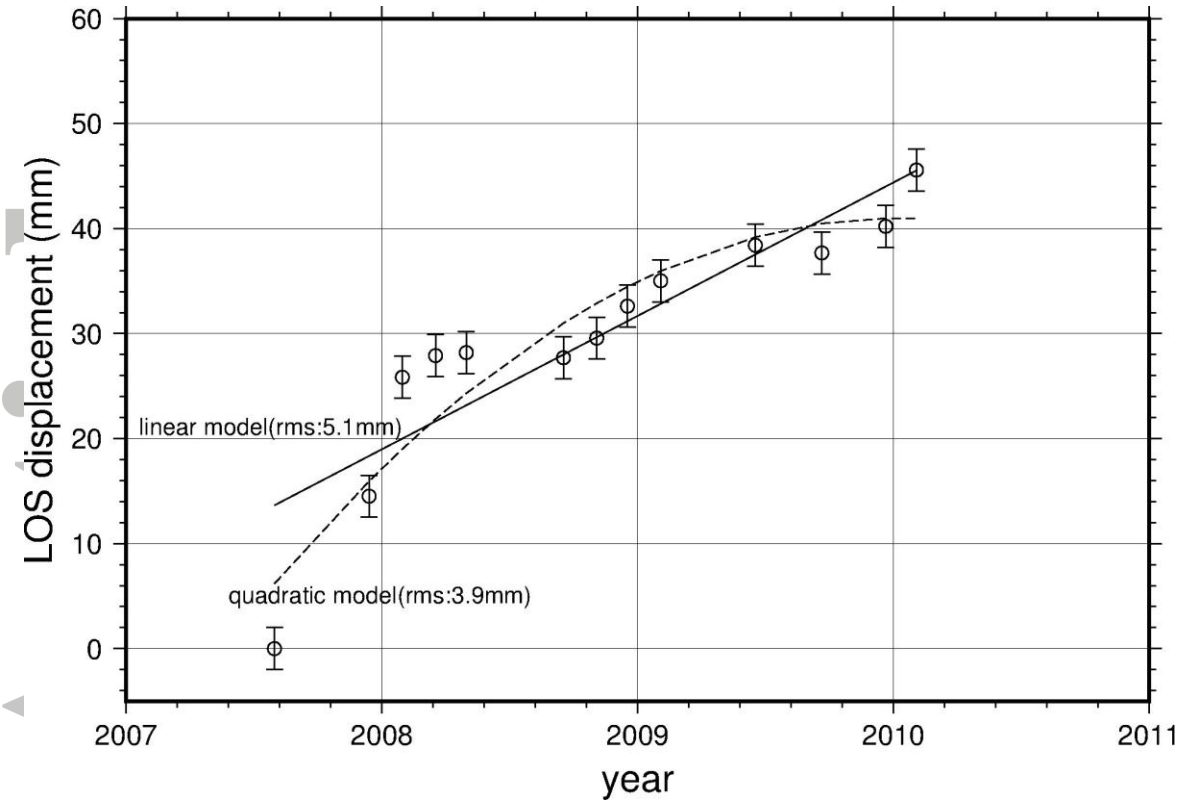

Figure 4. Relative InSAR LOS time-series data across the creeping Aceh segment of the Sumatran Fault. The data points are shown as open circles with error bars. The solid line is the best-fit linear model and the dash curve is the best-fit quadratic model. The misfits of the two models are also shown in the figure.